**Climate
of the Past**

Open Access

EGU

Supplement of

Analytical constraints on layered gas trapping and smoothing of atmospheric variability in ice under low-accumulation conditions

Kévin Fourteau et al.

Correspondence to: Kévin Fourteau (kevin.fourteau@univ-grenoble-alpes.fr) and Patricia Martinerie (patricia.martinerie@univ-grenoble-alpes.fr)

Table S1. Calibrated and measured methane mixing ratios of Scott Marrin Inc. standard gases.

Gas Reference	Calibrated value (pbbv)	Measured value (pbbv)
CB09722	703.90	695.5
CB09752	1789.42	1775.9
CB09754	360.09	355.3

S1. Calibration of methane measurements

S1.1 Calibration of SARA on NOAA2004 scale

The laser spectrometer used for the continuous methane measurements (SARA) was calibrated against the NOAA2004 scale (Dlugokencky et al., 2005) before starting the ice core analyzes. Three calibrated standard gases of known methane mixing ratios, listed Table S1, were measured with the SARA instrument. We derived a linear relationship between measured and calibrated mixing ratios over the range of 361 to 1790 pbbv, with a coefficient of determination R = 0.9999993. The data and regression line are displayed Fig. S1. This correction was applied to the SARA Vostok 4G-2 measurements.

S1.2 Correction for methane solubility

In the measurement line, once the ice core is melted, the liberated gases dissolve in the melt water. However, methane has a higher solubility than oxygen or nitrogen, and it follows that CH_4 dissolves preferentially, leading to reduced methane mixing ratios in the extracted air reaching the SARA spectrometer. The solubility correction was evaluated by comparing the Vostok signal with WAIS Divide ice core (WDC) data: a CFA record already corrected for solubility effects (Rhodes et al., 2015). The solubility factor was estimated by comparing the mean concentration over the plateau preceding the DO-17 event, unaffected by smoothing. This corresponds to a depth interval from 920 to 931 m in the Vostok ice core. The resulting solubility correction coefficient of 1.125, consistent with the previous estimate for our CFA system, was applied to the whole Vostok dataset.

S2. Quantification of the smoothing by the CFA system

Due to mixing and dead volumes, the CFA system introduces a smoothing of the gas signals. Using the method described in Stowasser et al. (2012), we measured the switch between two mixes of deionized water and standard gas (Fig. S2, left panel). It allowed us to determine the step response of the CFA system, which is not instantaneous but spreads over time. The observed step response was fitted using the cumulative density function of a log-normal distribution. This log-normal distribution (Fig. S2, middle panel) can be further used as a Green's function, or impulse response of the CFA system, to estimate the smoothing of other signals such as the simulated density-related concentration anomalies in Section 4.3 of the article. Finally, the Green's function can be used to derive the frequency response of the system using Fourier transform, that is to say the attenuation factor (also referred to as a gain) experienced by a sine signal depending on its frequency/period/wavelength. A cut-off wavelength can be defined as the wavelength of a sine signal experiencing a 50% attenuation in amplitude. For our CFA system with a melting rate of $3.8\,\mathrm{cm\,min^{-1}}$, the cut-off wavelength is about 2.4 cm. It is important to note that this cut-off is defined for sine signals, and therefore cannot be directly applied to other types of signals. For instance, a square spike with a width of 2.4 cm will not be attenuated by 50%. Indeed, it has a low-frequency rich harmonic content and thus undergoes a weaker attenuation. This explains why layered trapping artifacts with widths slightly below the cut-off wavelength used in Section 4.3 of the article are weakly damped in the CFA signal.

S3. Kerosene contamination

As explained in Section 3.1 of the article, traces of kerosene producing iridescent colors and a strong smell were occasionally detected in the meltwater. Concomitant increases in CH_4 and CO were assumed to result from kerosene contaminations. An example of such typical simultaneous increases is displayed on Fig. S3. Even though the origin of these kerosene contaminations
5   is not clear, they might come from cracks observed in the CFA sticks as seen in Fig. S4.

S4. Thin sections of the Vostok 4G-2 core

Four thin sections were prepared over a region of the Vostok 4G-2 ice core which shows layered trapping artifacts. The crystallographic orientations of grains were measured using an Automatic Texture Analyzer (Wilson et al., 2003; Peternell et al., 2010). The images were then segmented to visualize grain boundaries, using a high-pass filter and a threshold technique. Grain
10   boundaries were enhanced with cycles of dilate/erode. The segmented thin sections are displayed on Fig. S5. The numbers of intersections between grain boundaries and constant depth lines were computed as a metric for local grain size. However, the thin sections displayed various degrees of noise, impacting the number of intersection counted. To reduce the influence of noise, we normalized the numbers of intersections of each section by dividing them by the mean number of intersections of the whole thin section. This did not affect the interpretation of our results, as we were searching for local variations of grain
15   size rather than absolute size values. Figure S6 shows the methane record together with the normalized number of intersections around $902\,\mathrm{m}$ depth. The methane record presents two clear layered trapping artifacts, marked by red dots on Fig. S6. However, the grain size metric does not show a correlation with the two anomalous layers.

S5. Sensitivity of the layered trapping model

In Fig. S7 to S10, black solid lines correspond to normal trapping. Blue and yellow areas correspond to the expected extent
20   of layering artifacts, respectively for early and late closure. Spikes correspond to the artifacts for a stochastic realization of layered trapping with CFA smoothing. Blue spikes show early closure artifacts and yellow spikes late closure artifacts.

S6. AICC2012 gas chronology over the DO-017 event

Figure S11 presents the comparison between the WDC and Vostok methane records of the DO-17 event, using respectively the WD2014 and AICC2012 chronologies (Bazin et al., 2013; Veres et al., 2013; Buizert et al., 2015). Two dating method features
25   explain the differences with Fig. 5 of the article. First the WD2014 chronology is scaled by a factor 1.0063 with respect to the GICC05 chronology (with present defined as 1950), used in the AICC2012 synchronization (Buizert et al., 2015). Second the variability of AICC2012 ΔAge values shown in Fig. 2 of the article affect the duration of the events in the Vostok ice core.
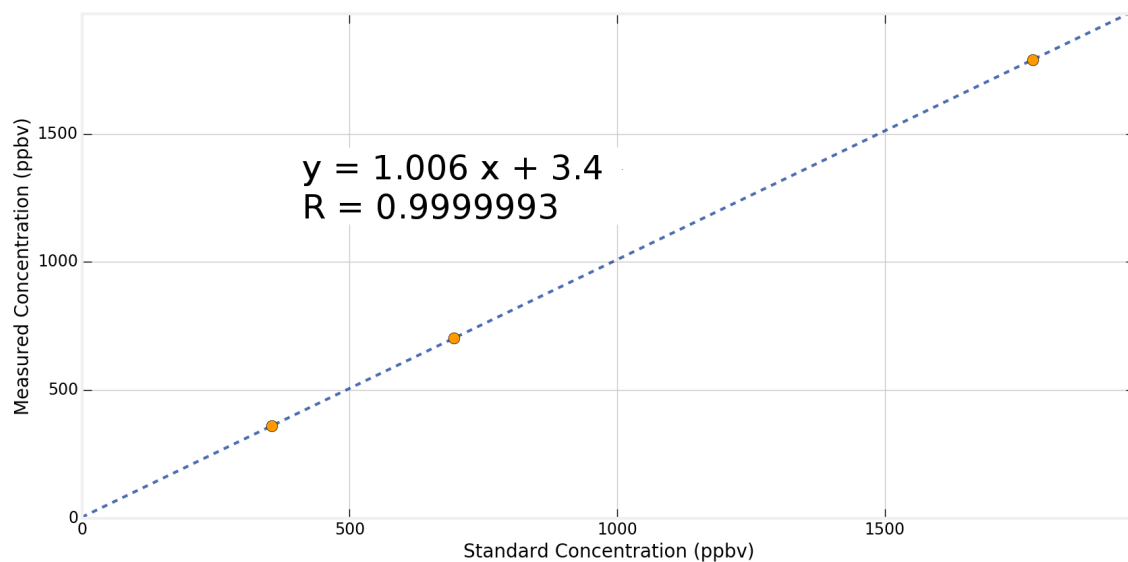
Figure S1. Linear regression between NOAA certified methane mixing ratios and SARA measurements. The blue dotted line is the regression, and the orange dots are measurements.
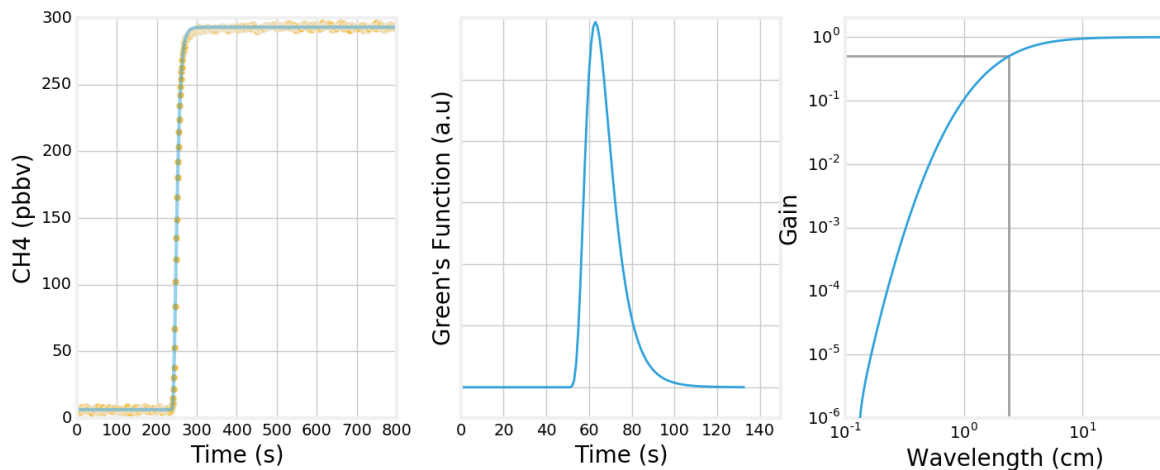

Figure S2. Left panel: step response of the CFA system. Orange dots: measurement points. In blue: fit by the cumulative density function of a log-normal law. Middle panel: Green's Function of the CFA system approximated by a log normal law. Right panel: Gain of the CFA system against the wavelength of sine signals. Gray lines correspond to the cut-off wavelength and a 50% attenuation.
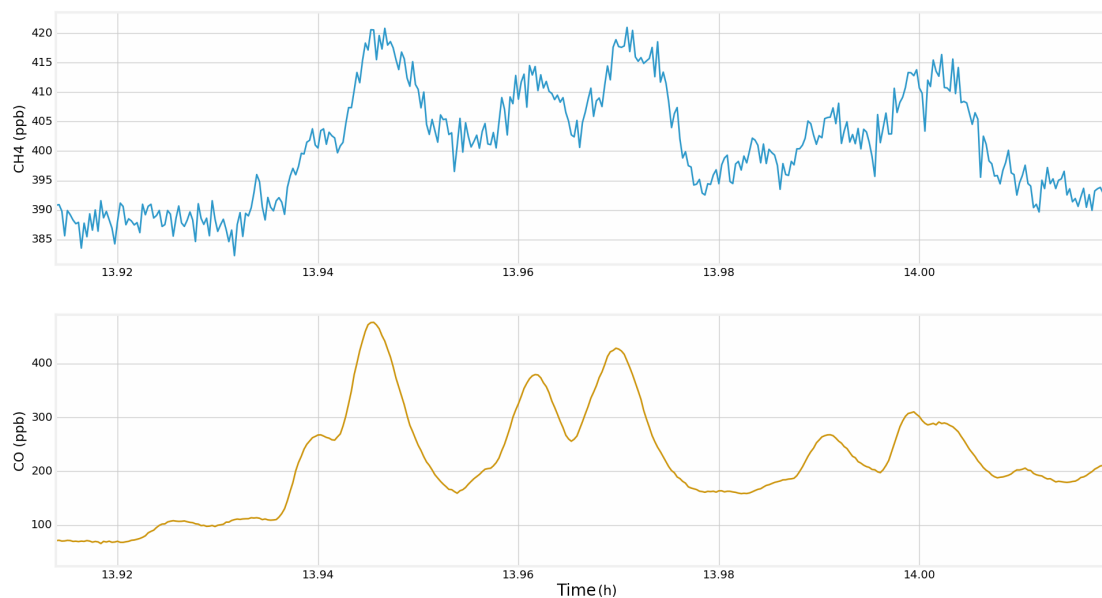
Figure S3. Example of concomitant increases in CH_4 and CO attributed to kerosene contamination. Methane (in blue) and carbon monoxide (in yellow) records display simultaneous fast variability. The x-scale represents the measurement time. The length of ice melted in the data shown is about $25\,cm$.
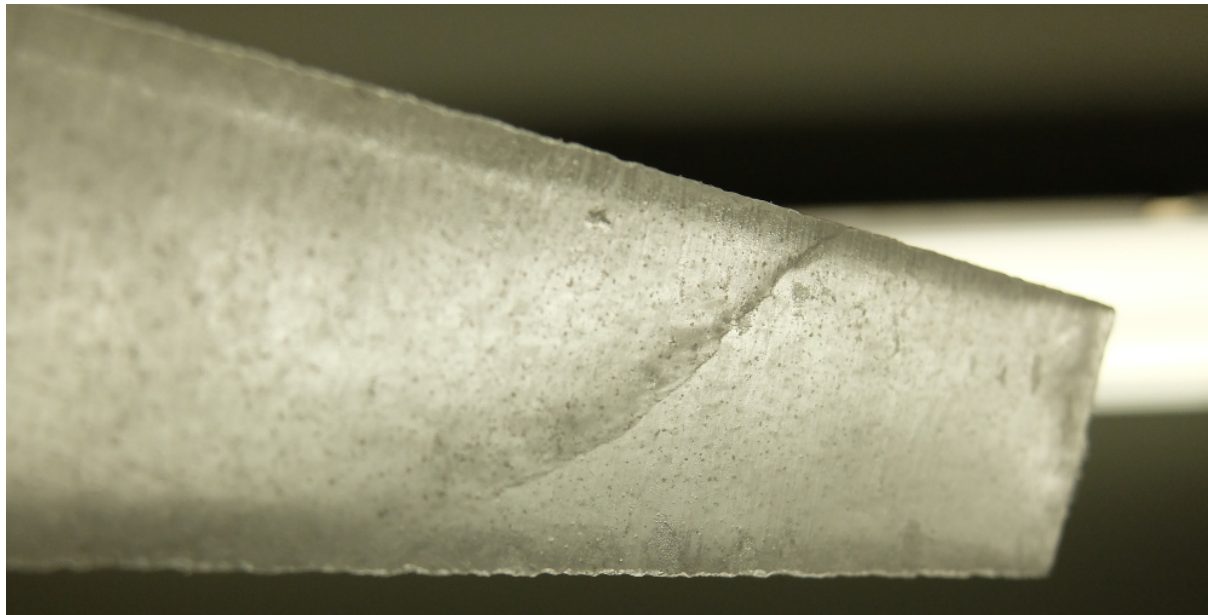

Figure S4. Pictures of a CFA stick. A large crack is visible in the middle, as well as relaxation cavities. Visual observations did not allow us to detect a variability in the ice aspect (e.g. cloudy bands, small fractures, or variability in the size and distribution of cavities) that could be associated with methane concentration anomalies.
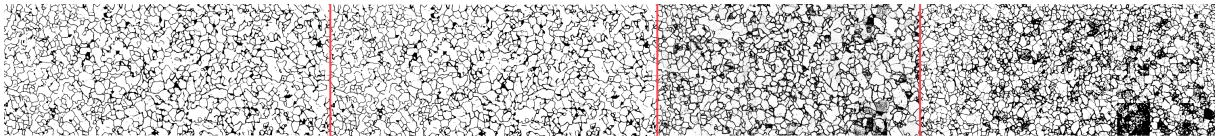
Figure S5. Segmented thin sections with grain boundaries shown in black. Individual thin sections are separated by red lines. The shallowest thin section is on the left. The total length of the four thin sections is about $40\,\mathrm{cm}$
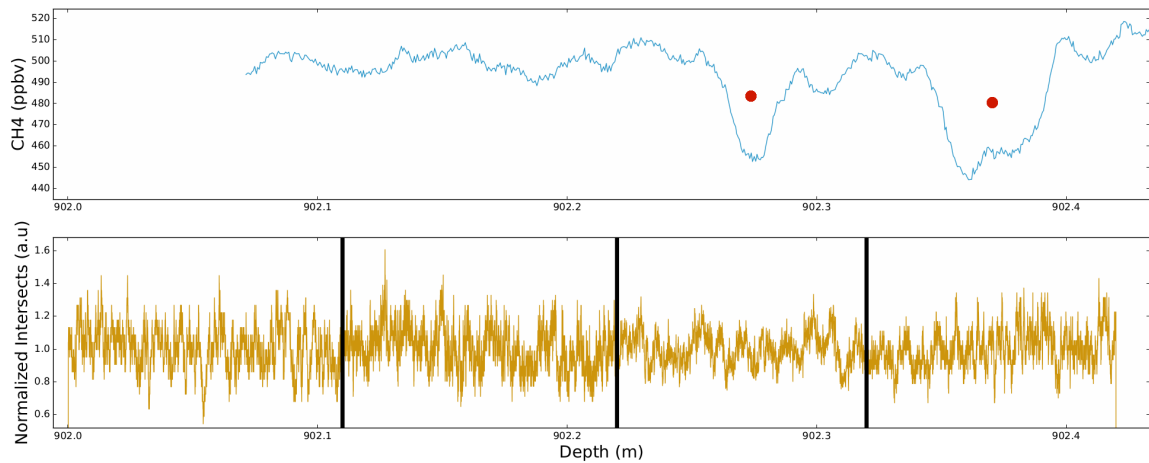

Figure S6. Top panel: continuous methane measurements with two anomalous layers marked by red dots. Bottom panel: normalized number of intersections along the thin sections. The different thin sections are separated by vertical black lines.
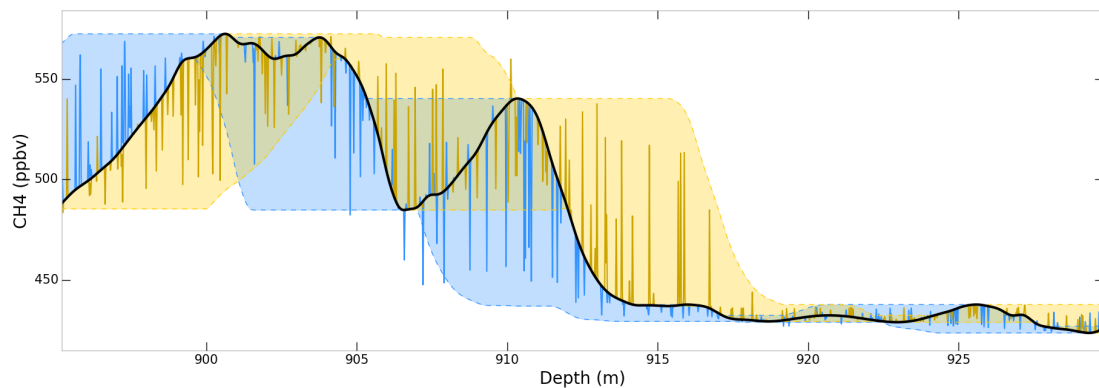

Figure S7. Layered trapping model without limitation for late closure age anomalies. Both shaded areas correspond to the range of concentration anomalies for early and late closure anomalies up to two standard deviations (depth anomaly of $5\,\mathrm{m}$ corresponding to an age anomaly of $415\,\mathrm{yr}$).

Figure S8. Layered trapping model with density anomalies standard deviation set to $3\,\mathrm{kg\,m^{-3}}$ and $d\rho/dz$ set to $2.5\,\mathrm{kg\,m^{-4}}$. Blue shaded areas correspond to the range of concentration anomalies for early closure anomalies up to two standard deviations (depth anomaly of $2.4\,\mathrm{m}$ corresponding to an age anomaly of $200\,\mathrm{yr}$). Yellow shaded areas correspond to late closure anomalies with 25% of the early closure extent (depth anomaly of $0.6\,\mathrm{m}$ corresponding to an age anomaly of $50\,\mathrm{yr}$).

Figure S9. Layered trapping model with density anomalies standard deviation set to $7\,\mathrm{kg\,m^{-3}}$ and $d\rho/dz$ set to $1.7\,\mathrm{kg\,m^{-4}}$. Blue shaded areas correspond to the range of concentration anomalies for early closure anomalies up to two standard deviations (depth anomaly of $8.2\,\mathrm{m}$ corresponding to an age anomaly of $684\,\mathrm{yr}$). Yellow shaded areas correspond to late closure anomalies with 25% of the early closure extent (depth anomaly of $2.1\,\mathrm{m}$ corresponding to an age anomaly of $171\,\mathrm{yr}$).

Figure S10. Layered trapping model with anomalous layers undergoing the WDC gas age distribution. The dashed black line corresponds to the WDC signal on the Vostok depth scale. Blue shaded areas correspond to the range of concentration anomalies for early closure anomalies up to two standard deviations (dept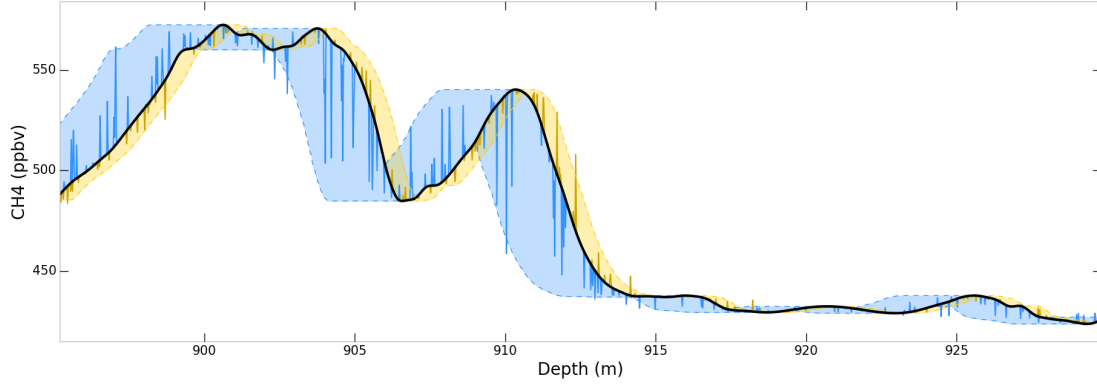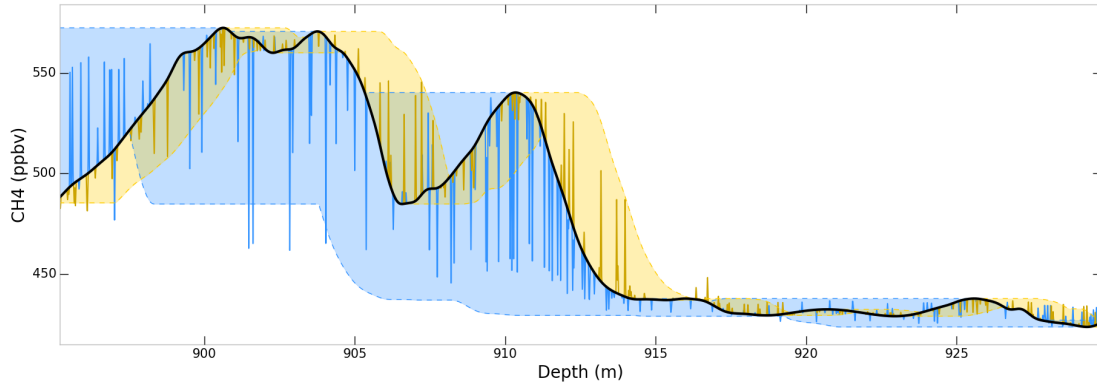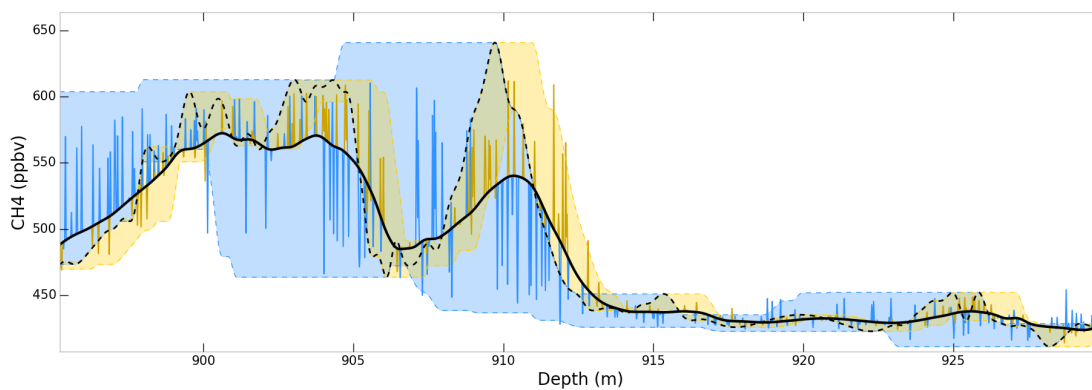h anomaly of 5 m corresponding to an age anomaly of 415 yr). Yellow shaded areas correspond to late closure anomalies with 25% of the early closure extent (depth anomaly of 1.25 m corresponding to an age anomaly of 104 yr).
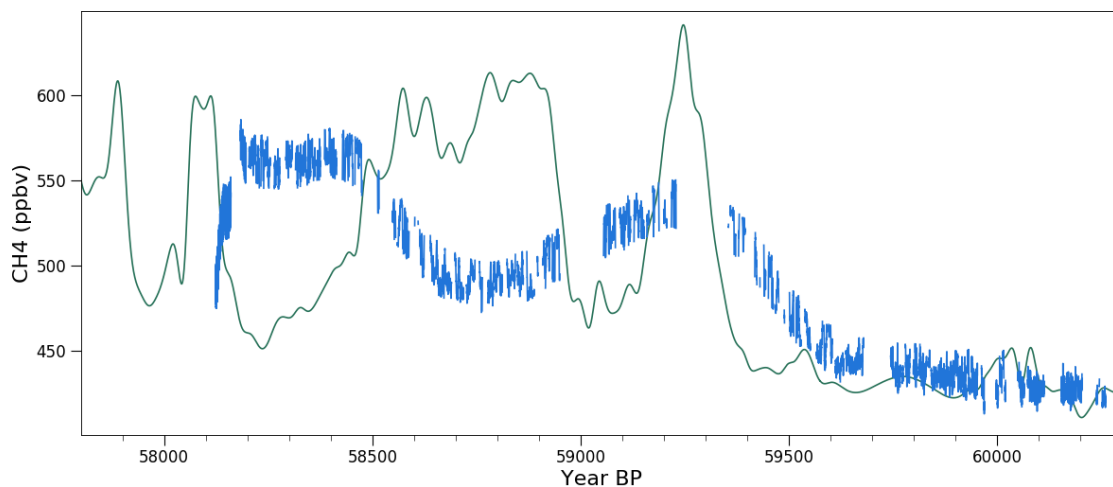

Figure S11. In green: WDC methane record with the WDC2014 gas chronology from Buizert et al. (2015). In blue: Vostok methane record with the AICC2012 gas chronology (Bazin et al., 2013; Veres et al., 2013).

References

Bazin, L., Landais, A., Lemieux-Dudon, B., Toyé Mahamadou Kele, H., Veres, D., Parrenin, F., Martinerie, P., Ritz, C., Capron, E., Lipenkov, V. Y., Loutre, M.-F., Raynaud, D., Vinther, B., Svensson, A., Rasmussen, S. O., Severi, M., Blunier, T., Leuenberger, M., Fischer, H., Masson-Delmotte, V., Chappellaz, J., and Wolff, E. W.: An optimized multi-proxy, multi-site Antarctic ice and gas orbital chronology (AICC2012): 120-800 ka, Clim. Past, 9, 1715–1731, https://doi.org/10.5194/cp-9-1715-2013, 2013.

5   Buizert, C., Cuffey, K. M., Severinghaus, J. P., Baggenstos, D., Fudge, T. J., Steig, E. J., Markle, B. R., Winstrup, M., Rhodes, R. H., Brook, E. J., Sowers, T. A., Clow, G. D., Cheng, H., Edwards, R. L., Sigl, M., McConnell, J. R., and Taylor, K. C.: The WAIS Divide deep ice core WD2014 chronology-Part 1: methane synchronization (68-31 ka BP) and the gas age-ice age difference, Clim. Past, 11, 153–173, https://doi.org/10.5194/cp-11-153-2015, 2015.

Dlugokencky, E. J., Myers, R. C., Lang, P. M., Masarie, K. A., Crotwell, A. M., Thoning, K. W., Hall, B. D., Elkins, J. W., and Steele, L. P.:
10   Conversion of NOAA atmospheric dry air CH_4 mole fractions to a gravimetrically prepared standard scale, J. Geophys. Res.-Atmos., 110, https://doi.org/10.1029/2005jd006035, 2005.

Peternell, M., Russell-Head, D., and Wilson, C.: A technique for recording polycrystalline structure and orientation during in situ deformation cycles of rock analogues using an automated fabric analyser, J. Microsc.-Oxford, 242, 181–188, https://doi.org/10.1111/j.1365-2818.2010.03456.x, 2010.

15   Rhodes, R. H., Brook, E. J., Chiang, J. C. H., Blunier, T., Maselli, O. J., McConnell, J. R., Romanini, D., and Severinghaus, J. P.: Enhanced tropical methane production in response to iceberg discharge in the North Atlantic, Science, 348, 1016–1019, https://doi.org/10.1126/science.1262005, 2015.

Stowasser, C., Buizert, C., Gkinis, V., Chappellaz, J., Schüpbach, S., Bigler, M., Faïn, X., Sperlich, P., Baumgartner, M., Schilt, A., and Blunier, T.: Continuous measurements of methane mixing ratios from ice cores, Atmos. Meas. Tech., 5, 999–1013, https://doi.org/10.5194/amt-5-999-2012, 2012.

20   Veres, D., Bazin, L., Landais, A., Toyé Mahamadou Kele, H., Lemieux-Dudon, B., Parrenin, F., Martinerie, P., Blayo, E., Blunier, T., Capron, E., Chappellaz, J., Rasmussen, S. O., Severi, M., Svensson, A., Vinther, B., and Wolff, E. W.: The Antarctic ice core chronology (AICC2012): an optimized multi-parameter and multi-site dating approach for the last 120 thousand years, Clim. Past, 9, 1733–1748, https://doi.org/10.5194/cp-9-1733-2013, 2013.

25   Wilson, C. J. L., Russell-Head, D. S., and Sim, H. M.: The application of an automated fabric analyzer system to the textural evolution of folded ice layers in shear zones, Ann. Glaciol., 37, 7–17, https://doi.org/10.3189/172756403781815401, 2003.